

# Measurement of intrinsic alignments in galaxy ellipticities

M.L. Brown<sup>1</sup>, A.N. Taylor<sup>1</sup>, N.C. Hambly<sup>1</sup> & S. Dye<sup>2</sup>

<sup>1</sup> *Institute for Astronomy, University of Edinburgh, Royal Observatory, Blackford Hill, Edinburgh, U.K.*

<sup>2</sup> *Astrophysics Group, Blackett Lab, Imperial College, Prince Consort Road, London, U.K.*

*mlb@roe.ac.uk, ant@roe.ac.uk*

1 December 2018

## ABSTRACT

We measure the alignment of galaxy ellipticities in the local Universe over a range of scales using digitized photographic data from the SuperCOSMOS Sky Survey. We find for a magnitude cut of  $b_J < 20.5$ , corresponding to a median galaxy redshift of  $z \approx 0.1$ , and  $2 \times 10^6$  galaxies, that the galaxy ellipticities exhibit a non-zero correlation over a range of scales between 1 and 100 arcminutes. In particular, we measure the variance of mean galaxy ellipticities,  $\sigma^2(\theta)$ , in square angular cells on the sky as a function of cell size and find it lies in the range,  $2 \times 10^{-4} \geq \sigma^2(\theta) \geq 1 \times 10^{-5}$  for cell side lengths between  $15 \leq \theta \leq 100$  arcminutes. Considering the low median redshift of the galaxies in the sample and hence the relatively low effective cross-section for lensing of these galaxies by the large-scale structure of the Universe, we propose that we have detected an intrinsic alignment of galaxy ellipticities. We compare our results to recent analytical and numerical predictions made for the intrinsic galaxy alignment and find good agreement. We discuss the importance of these results for measuring cosmic shear from upcoming shallow surveys (e.g. Sloan Digital Sky Survey) and we outline how these measurements could possibly be used to constrain models of galaxy formation and/or measure the mass distribution in the local universe.

**Key words:** cosmology: observations - gravitational lensing - large-scale structure, galaxies: formation

## 1 INTRODUCTION

Over the last decade, considerable interest has been directed towards the measurement and analysis of galaxy ellipticities as a means to estimate shear induced by gravitational lensing (see e.g. Bartelmann & Schneider 1999). On the scale of galaxy clusters, this is now a well-established method, with tools to invert the shear pattern and measure the distribution of Dark Matter. Recently attention has moved to larger scales to measure the cosmological weak shear signal of lensing by large-scale structure and a number of groups have made consistent detections (Bacon, Refregier & Ellis 2000; Kaiser, Wilson & Luppino 2000; van Waerbeke et al. 2000; Wittman et al. 2000). Despite the remarkable success of the shear analysis, up until recently very little attention had been paid to the prospect of intrinsic alignments mimicking the gravitational shear signal. The most likely ways for this to occur is during the tidally induced spin-up of galaxies (Hoyle 1949), where the angular momentum axes, and hence ellipticities, are aligned, or through the alignment of galaxy and halo shapes.

Over the last year, this problem has been addressed by a number of groups using a combination of numerical (Heavens, Refregier & Heymans 2000, Croft & Metzler 2001)

and analytic methods (Catelan, Kamionkowski & Blandford 2001, Crittenden et al 2001). Although these results are in rough agreement, a complete understanding of alignments is less secure, with the main problems lying in understanding the coupling of the tidal and inertial tensors of dark matter haloes, and the alignment of galaxies and haloes. On the observational side Pen, Lee & Seljak (2000) have recently claimed a weak detection of spin-spin correlations in the Tully catalogue. In this letter we have measured the variance of ellipticities of galaxies at low-redshift, where the effect of intrinsic alignments is predicted to be orders of magnitude higher than a lensing effect. These observations may help to distinguish between models for alignments.

This paper is laid out as follows. In Section 2 we present the observational material used in the analysis. In Section 3 the main analysis methods are introduced, and our results are presented in Section 4, where we discuss the significance of our results. Our conclusions are presented in Section 5.

## 2 OBSERVATIONAL MATERIAL

The observations analysed in this paper are taken from the SuperCOSMOS Sky Survey program (Hambly et al. 2001a).

This digitised photographic sky survey consists of Schmidt photographic plates ( $6^\circ \times 6^\circ$ ; plate scale, 1 cm = 11.2') and covers the entire southern sky (894 individual Schmidt fields) in two colours, b<sub>J</sub> and R. The material used in this analysis consisted of 436 Schmidt plates corresponding to  $\sim 10,000$  square degrees.\*

We have constructed an object catalogue (including both stars and galaxies) for the 436 fields by pairing the scanned b<sub>J</sub> and R plates. Apart from a small number of large overlap regions near the 0<sup>h</sup> boundary in the survey which were used for internal consistency checks (see Section 3.4), we created a ‘seamless’ catalogue from the overlapping plates using the scheme described in Hambly et al. (2001a). This scheme attempts to include the image with the best parameters (and exclude the others) when there is a choice to be made for the same image appearing on more than one plate. Pairing the b<sub>J</sub> and R plates has the advantage over single-colour catalogues in that spurious objects on one plate are eliminated. This is particularly important for galaxy studies from Schmidt photographs since these defects are broken up into many co-aligned ‘galaxies’ by the image analyser. Such a large source of contaminants could potentially ruin any shear analysis.

Regions around bright stars and blended (ie. multiple) images have been excluded from the object catalogue to further eliminate spurious and/or poorly parameterised images. Further details concerning image parameterisation, classification and photometry are given in Hambly et al. (2001b). Image parameters included in the final object catalogue generated for this study consisted of (for both the b<sub>J</sub> and R bands) celestial co-ordinates, local plate co-ordinates, second-order moments (semi-major/minor axes and celestial position angle, see Section 3.1), b<sub>J</sub> and R magnitudes, (b<sub>J</sub>–R) colour, image classification flag and stellarness index. The external reliability of the image classification on the J plates is demonstrated in Hambly et al. (2001b) as  $\geq 92\%$  reliable for b<sub>J</sub>  $< 20.5$  with completeness at around  $\sim 97\%$ . Photometric accuracy for galaxies is around 0.25 mag. The internal consistency and accuracy in image ellipticity parameters is demonstrated later in Section 3.4.

### 3 ANALYSIS METHODS

#### 3.1 Measuring the ellipticities

In order to measure the intrinsic alignment of galaxies, we first divide the survey into square cells of angular side length,  $\theta$ . We define the mean ellipticity of galaxies within each cell,  $e_i$ , as

$$\begin{aligned} \bar{e}_{1,i} &= \frac{1}{N} \sum_{j=1}^N e_{1,j}, & \bar{e}_{2,i} &= \frac{1}{N} \sum_{j=1}^N e_{2,j}, \\ e_i^2 &= \bar{e}_{1,i}^2 + \bar{e}_{2,i}^2, \end{aligned} \quad (1)$$

where  $N$  is the number of galaxies in the  $i^{\text{th}}$  cell and  $e_{1,j}$  and  $e_{2,j}$  are the ellipticity components of the  $j^{\text{th}}$  galaxy which are defined with respect to the cell axes as

$$e_{\alpha,j} = \frac{a_j^2 - b_j^2}{a_j^2 + b_j^2} \begin{cases} \cos 2\varphi_j & \alpha = 1 \\ \sin 2\varphi_j & \alpha = 2 \end{cases}. \quad (2)$$

Here,  $a$  and  $b$  are the semi-major and semi-minor axes of the galaxy and  $\varphi$  is the orientation of the semi-major axis with respect to the cell axes. The weighting scheme used is  $w_i = H(I_i - I_{th})$  where  $I_i$  is the measured intensity in pixel  $i$ ,  $I_{th}$  is a threshold intensity corresponding to the sky background and  $H$  is the Heaviside step function. That is, the SuperCOSMOS analyser measures second moments for each object detected as (Stobie, 1986)

$$\begin{aligned} Q_{xx} &= \int d^2\theta w_i I(\theta) (\theta_x - \bar{\theta}_x)^2 / \int d^2\theta w_i I(\theta), \\ Q_{xy} &= \int d^2\theta w_i I(\theta) (\theta_x - \bar{\theta}_x)(\theta_y - \bar{\theta}_y) / \int d^2\theta w_i I(\theta), \\ Q_{yy} &= \int d^2\theta w_i I(\theta) (\theta_y - \bar{\theta}_y)^2 / \int d^2\theta w_i I(\theta), \end{aligned} \quad (3)$$

where  $\bar{\theta}_x$  and  $\bar{\theta}_y$  are the centroids of the object and are given by

$$\begin{aligned} \bar{\theta}_x &= \int d^2\theta \theta_x w_i I(\theta) / \int d^2\theta w_i I(\theta), \\ \bar{\theta}_y &= \int d^2\theta \theta_y w_i I(\theta) / \int d^2\theta w_i I(\theta). \end{aligned} \quad (4)$$

In terms of second moments, the ellipticity components of equation (2) are

$$\begin{aligned} e_1 &= \frac{Q_{xx} - Q_{yy}}{Q_{xx} + Q_{yy}}, \\ e_2 &= \frac{2Q_{xy}}{Q_{xx} + Q_{yy}}. \end{aligned} \quad (5)$$

The weighting scheme used corresponds to measuring unweighted second moments within an isophotal threshold for all the objects detected. We have varied this threshold limit and have found the resulting measurements to be largely insensitive to the isophotal threshold used (see Section 4.2). To quantify the degree of alignment of the cell ellipticities, we calculate the variance of  $e_i$  on a given scale across the entire survey. Since this statistic has been used to measure cosmic shear (e.g. Bacon et al., 2000, Kaiser et al., 2000), we can directly compare the contributions of intrinsic and extrinsic galaxy alignments. In order to obtain an accurate estimate of  $e_i$  for a cell, a number of corrections to the raw image catalogue are required. We now describe the sources of error on the ellipticity measurements of galaxies and the corrections we have applied to the dataset.

#### 3.2 Correction for PSF anisotropy

There are several possible sources of error which could potentially compromise any shear analysis. These distortions result in spurious ellipticities for all the objects detected and must be removed before a shear analysis can be performed. Firstly, there may be slight astrometric distortions present in the dataset due to emulsion shifts in the photographic plates. However, these should be negligible — the dataset we have used has very precise astrometry and has been used as a standard for making astrometric corrections in other shear analyses (e.g. Gray et al., 2001). We have therefore not corrected for astrometric distortions in this analysis. For

\* Full details and online access to the data are available via the World Wide Web at URL <http://www-wfau.roe.ac.uk/sss>

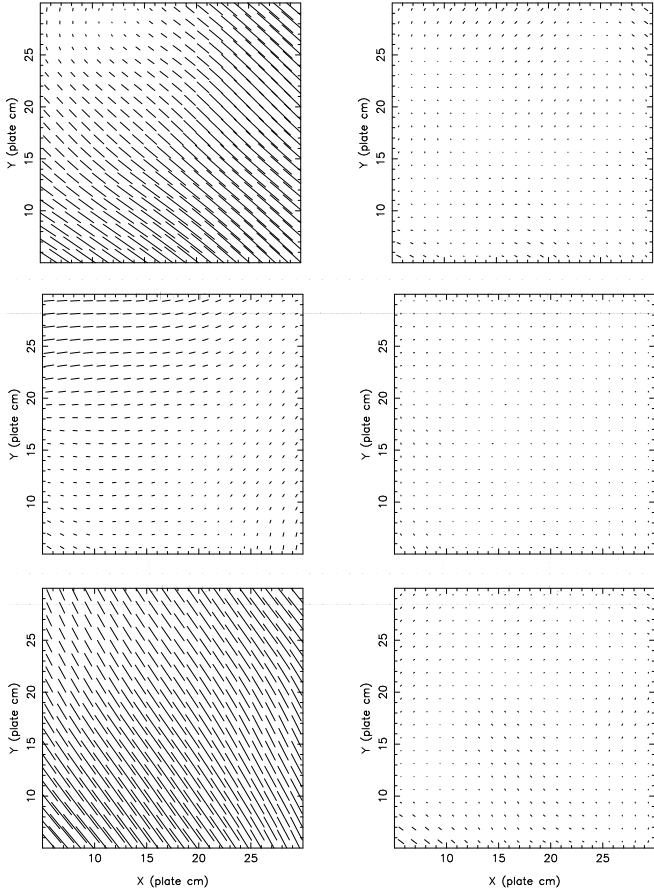


**Figure 1.** Ellipticity fields for raw (LHS) and corrected (RHS) stars for three of the  $b_J$ -band SuperCOSMOS fields. Stars are binned into cells of a side  $10'$  and smoothed with a Gaussian with a smoothing scale  $15'$ . For each plot, the length of each vector drawn is 25 cm times the measured cell ellipticity. The average ellipticity in a cell in the raw fields is  $\bar{e} \approx 10^{-2}$ , while the average ellipticity in a corrected cell is  $\bar{e} \approx 10^{-4}$ . These plots are typical for the PSF anisotropy distributions on a plate and the corresponding R-band plots are generally very similar.

a detailed discussion of the astrometric accuracy of the catalogue, see Hambly et al., 2001c.

The first correction we have made to the dataset is a correction for anisotropy in the point spread function (PSF). There are several sources of error contributing to the PSF anisotropy. Atmospheric dispersion along with emulsion shifts and mechanical plate distortions, are minor contributors to the PSF anisotropy. By far the most important factors, however, are tracking errors and field rotation (for an analysis of the alignment, pointing accuracy and field rotation of the UK Schmidt Telescope, see Wallace & Tritton, 1979; further details of the telescope optics are given in Wynne, 1981). These effects combine to produce a systematic PSF anisotropy pattern across each plate which needs to be corrected for before the galaxy ellipticity measurements can be trusted. We have done this by comparing with the ellipticity field for the stars. Stars should have no intrinsic ellipticity and so the measured stellar ellipticities are due to the PSF anisotropy. As shown in Kaiser, Squires and Broadhurst, 1995 (hereafter, KSB), the perturbation to the galaxies' ellipticity components is given by

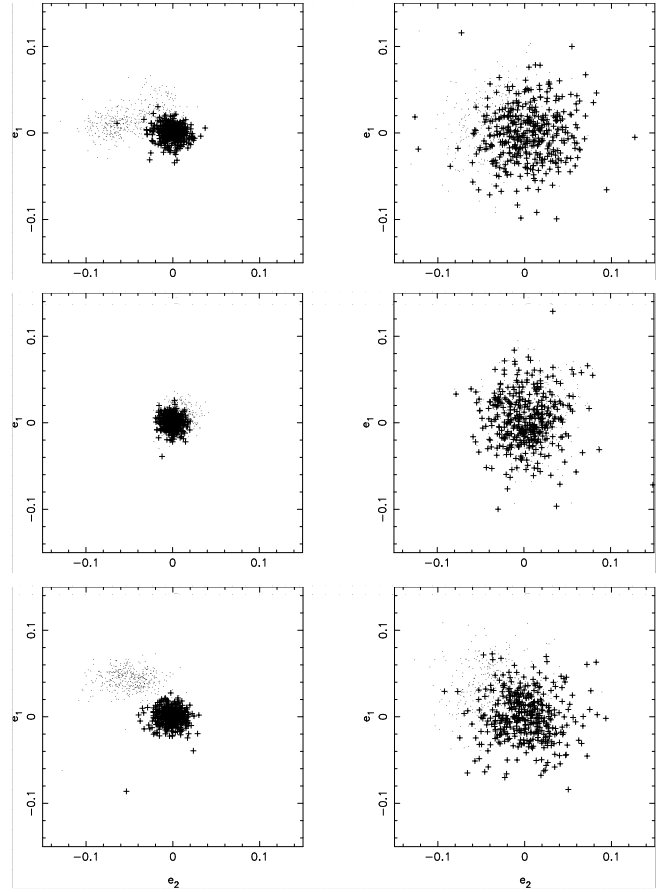


**Figure 2.** Ellipticity distribution per cell (stars on the left, galaxies on the right) for the same three  $b_J$ -band fields shown in figure 1. The dots are the raw stars/galaxies, the crosses the corrected values. Each cell has an ellipticity estimated from equation (1) and has an uncertainty given by equation (15). Average stellar distortions in the raw fields of  $\bar{e}_1 \sim \bar{e}_2 \approx 10^{-2}$  are corrected to produce flattened stellar ellipticity distributions with residual ellipticities,  $\bar{e}_1 \sim \bar{e}_2 \approx 10^{-4}$ . Similar “before” and “after” distributions are found for the R plates.

$$\delta e_\alpha = P_{\alpha\beta}^s p_\beta, \quad (6)$$

where  $P_{\alpha\beta}^s$  is the “smear polarizability tensor” which describes the response of the individual galaxy images to the PSF anisotropy,  $p_\alpha$  which in turn can be measured from the stars. The analysis described in KSB, which is for a general weighting of quadrupole moments, is to measure the quantities,  $P_{\alpha\beta}^s$  for each individual galaxy and  $p_\alpha$  from the foreground stars and to apply the correction in equation (6) to the individual galaxies. However, for the essentially unweighted moments that we have made use of in our analysis (see Section 3.1),  $P_{\alpha\beta}^s$  is diagonal with  $P_{11}^s = P_{22}^s$  being a measure of the inverse galaxy size and the KSB correction reduces to

$$\delta e_\alpha = \frac{Q_{xx}^* + Q_{yy}^*}{Q_{xx} + Q_{yy}} e_\alpha^*, \quad (7)$$

where the  $Q^*$ 's and the  $Q$ 's are stellar and galaxy second moments respectively and  $e_\alpha^*$  are the measured stellar ellipticity components. In terms of semi-major and semi-minor axes, this becomes

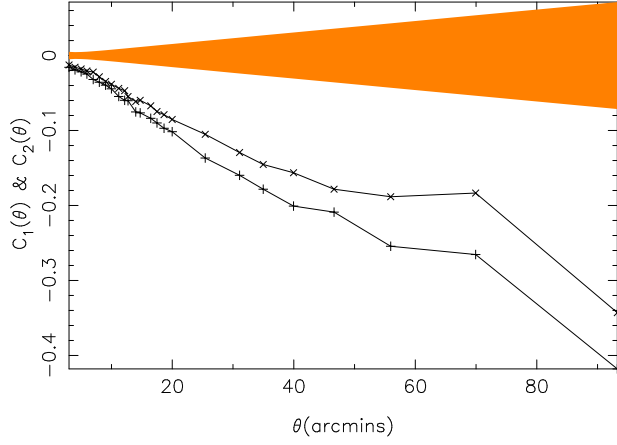


**Figure 3.** The linear correlation coefficients,  $C_1$  and  $C_2$  of the cell-averaged stellar and galaxy ellipticity components as described in the text, after correction for PSF anisotropy. The shaded region is the  $3\sigma$  significance level.

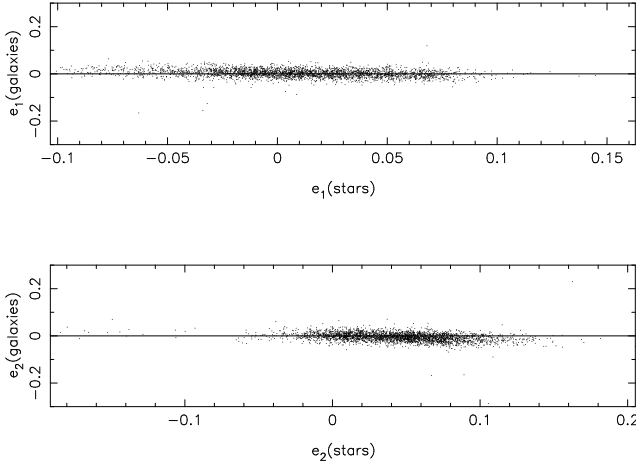


**Figure 4.** The observed anti-correlation of corrected galaxy cell ellipticity components ( $e_1$  on top,  $e_2$  on bottom) with the corresponding observed stellar ellipticities.

$$\delta e_\alpha = \frac{a^{*2} + b^{*2}}{a^2 + b^2} e_\alpha^* \quad (8)$$

where again, the superscript refers to the stars. We have applied the correction in equation (8) to individual galaxy ellipticities using cell-averaged measurements for the “stellar size” ( $a^{*2} + b^{*2}$ ), and where the  $e_\alpha^*$ ’s are the average stellar ellipticity components in the cell. The size of the cells used for this correction was  $10 \times 10$  arcmins.

To perform the correction, the plates are gridded up and an average stellar ellipticity is calculated for each cell in the grid. This ellipticity field is then Gaussian smoothed across the plate. Different smoothing scales were investigated in order to find an optimum value. The resulting measurements however did not change significantly for smoothing scales between 10 and 30 arcmins. The individual galaxy ellipticities are then corrected according to equation (8). If the grid used for smoothing is too small, a coherent distortion pattern cannot be made and an essentially random pattern is generated. Figure 1 illustrates the  $b_j$  band stellar ellipticities on three plates before and after this correction. A strong, coherent distortion of  $\bar{e} \approx 10^{-2}$  is corrected to produce a ran-

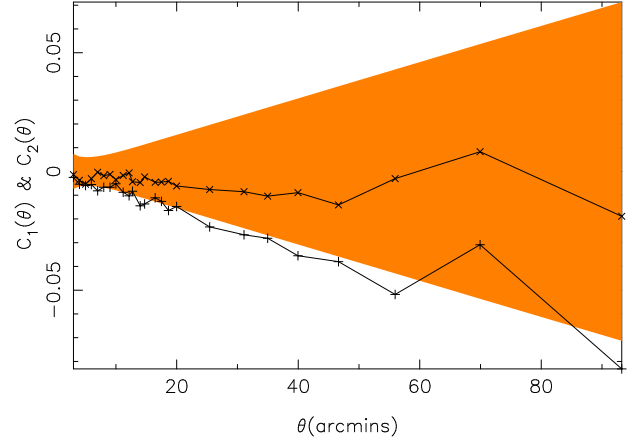


**Figure 5.**  $C_1$ ,  $C_2$  and the  $3\sigma$  significance level after excluding all galaxies with sizes,  $\theta_g < 0.8 \langle \theta_g \rangle$  from the catalogue.

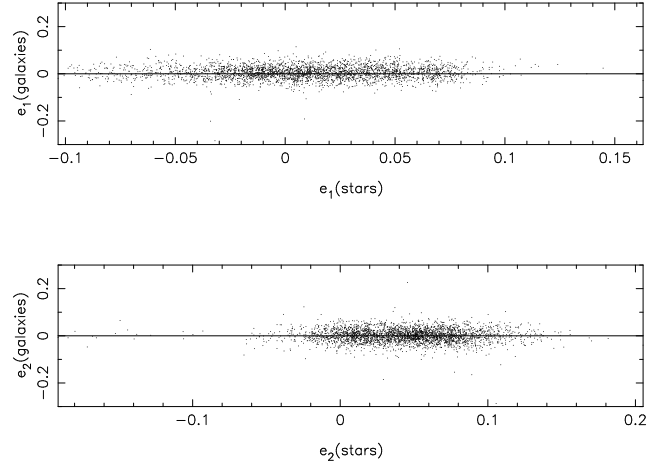


**Figure 6.** Cell-averaged galaxy ellipticity components ( $e_1$  top,  $e_2$  bottom) plotted as a function of the corresponding stellar ellipticities after applying the galaxy size cut described in the text.

dom ellipticity pattern with mean  $\bar{e} \approx 10^{-4}$ . Figure 2 shows a scatter plot of the ellipticities ( $e_1$  vs.  $e_2$ ) for both stars (LHS) and galaxies (RHS) before (dots) and after (crosses) correction. Each point corresponds to a cell, with an ellipticity value given by equation (1), and an uncertainty given by equation (15).

To test the success of the PSF correction further we calculated the linear correlation function of the cell-averaged stellar and galaxy ellipticity components (c.f. Bacon et al., 2000),

$$C_i = \frac{\langle e_\alpha^* e_\alpha \rangle - \langle e_\alpha^* \rangle \langle e_\alpha \rangle}{\sigma(e_\alpha^*) \sigma(e_\alpha)}, \quad (9)$$

where  $e_\alpha^*$  and  $e_\alpha$  are the cell-averaged stellar and galaxy ellipticity components respectively and  $\sigma(e_\alpha^*)$  and  $\sigma(e_\alpha)$  are the errors on those two quantities as measured from the data. In Figure 3, we plot  $C_1$  and  $C_2$  as measured from the total data set after correction for PSF anisotropy along with the  $3\sigma$  significance level. It can be seen from this figure that there is a clear anti-correlation between the corrected galaxies and the raw stars and furthermore, it is a  $\gg 3\sigma$  effect,

especially at large bin sizes. This anti-correlation is clearly seen in Figure 4 where we plot the corrected galaxy and raw stellar ellipticity components for a bin size of  $\theta = 70$  arcmins. This anti-correlation is the same effect seen in the cosmic shear analysis of Bacon et al. (2000) and is due to an over-correction of the PSF anisotropy for small galaxies. To remove this effect, we have imposed a cut on galaxy size, only taking galaxies with  $\theta_g > 0.8 \langle \theta_g \rangle$ , where  $\theta_g = a^2 + b^2$  is the individual galaxy size, and  $\langle \theta_g \rangle$  is the mean galaxy size over the whole survey. Only galaxies satisfying this condition have been used in the final analysis. The correlation functions, equation (9), calculated after applying this cut, are shown in Figure 5. It is clear from this figure that the star-galaxy anti-correlation is no longer significant at the  $3\sigma$  level and this can be seen by eye in Figure 6 where the corrected galaxy and raw stellar ellipticity components are plotted after applying the cut on galaxy size, again for a bin size of 70 arcmins.

### 3.3 Seeing correction

After correcting for PSF anisotropy, we model all other sources of error (atmospheric turbulence, wind shake etc.) as random effects. Collectively called seeing, we assume also it is isotropic and we apply a stochastic correction to remove its effects. The effect of seeing on the galaxy ellipticities is to circularize the images, causing a decrease in ellipticities. The seeing across all of the plates is typically  $2''$ . This is comparable to the size of a galaxy near the magnitude limit of our survey ( $b_J < 20.5$ ) and thus, needs to be corrected for before the galaxy ellipticities can be trusted.

We assume that the semi-major and semi-minor axes of each galaxy transform under the effect of seeing as

$$a_j'^2 = a_j^2 + r_i^2, \quad b_j'^2 = b_j^2 + r_i^2, \quad (10)$$

where  $(a_j, b_j)$  and  $(a_j', b_j')$  are the axes of the  $j^{\text{th}}$  galaxy before and after the effect of seeing respectively and  $r_i$  is the average seeing in the  $i^{\text{th}}$  plate. The average galaxy profile as measured using the SuperCOSMOS machine deviates from Gaussianity only very slightly (see Knox et al., 1998) and so equation (10) should describe the effect of seeing on the galaxy images reasonably accurately.

The effect of seeing on the measured ellipticities is

$$e'_{\alpha,j} = f_{ij} e_{\alpha,j}, \quad (11)$$

where  $e'_{\alpha,j}$  is the post-seeing ellipticity and we have defined a “seeing factor” which is, in terms of the observed semi-major and semi-minor axes,

$$f_{ij} = 1 - \frac{2r_i^2}{a_j'^2 + b_j'^2}. \quad (12)$$

Here,  $a$  and  $b$  are the axes of the galaxies after correction for PSF anisotropy and the uncertainty on individual galaxy sizes was too large after this correction to use equation (11) directly. Instead we estimated an effective galaxy size for all plates for a given flux cut. We have done this by looking at plate overlap regions. We have applied the correction in equation (11) to galaxies in these regions and have “fine tuned” the effective galaxy size so that consistency is achieved in the measurement of both individual and binned galaxy ellipticities between the overlapping plates (see Section 3.4). In the case of  $b_J \leq 20.5$ , the optimum effective

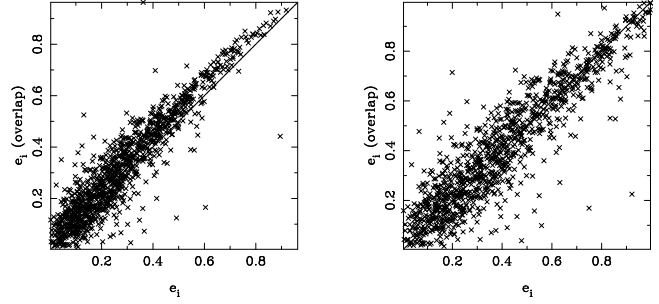


**Figure 7.** Individual galaxy ellipticities measured from overlapping SuperCOSMOS fields. The left-hand panel shows the ellipticity measurements before the seeing correction is applied. The plate plotted on the horizontal scale has greater seeing than the plate plotted on the vertical axis. The right hand panel shows the ellipticities after the correction.

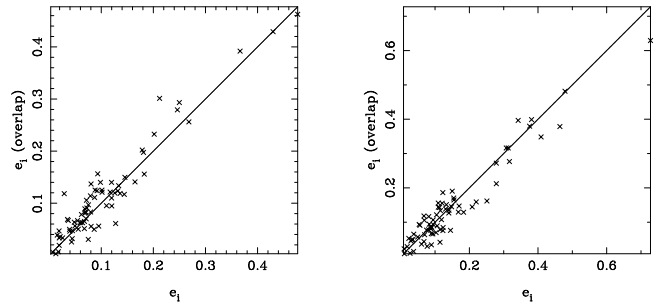


**Figure 8.** Binned cell ellipticities,  $e_i$  measured from the same plates as shown in Figure 3. The left-hand and right hand panel are the measurements before and after the seeing correction is applied respectively.

galaxy size was  $2.5''$ , which closely matched the directly measured mean galaxy size. This was then used to correct all the plates, using the measured seeing from each plate.

### 3.4 Internal consistency tests

We have tested the seeing correction of the previous section by comparing ellipticity measurements in the plate overlap regions. The ellipticity measurements for a galaxy in an overlap region as measured on the two overlapping plates should agree to within the limits of the measuring process (the measurement errors are dominated by noise on the original photographs) assuming that we have corrected for the effect of seeing accurately enough.

Figures 7 and 8 show the correlation between different plates in the overlap region, after correction for PSF anisotropy, for individual galaxies (Fig. 7) and binned cells (Fig. 8). The left-hand-side of Figures 7 and 8 show the correlation before correcting for seeing. There is an apparent decrease in the ellipticities of the galaxies plotted on the horizontal axis, where the seeing on the plate is larger. The right-hand-side of Figures 7 and 8 show the correlation after correction for seeing. As we are only scaling ellipticities the scatter is slightly increased, but the correlation is significantly greater. These plots are typical for the overlap regions.

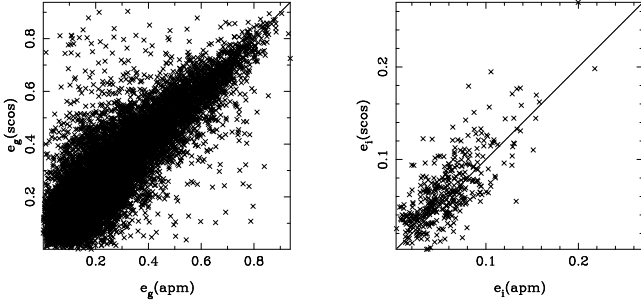


**Figure 9.** LHS: Scatter plot of the SuperCOSMOS galaxy ellipticities on a plate against those from the APM galaxy survey. RHS: The same as the LHS but for binned cells.

### 3.5 Comparison with APM Sky Catalogue data

To check our results further, we have performed a comparison test for similar alignments in APM data<sup>†</sup> in order to test for any systematic effects introduced by the SuperCOSMOS scanning procedure. We took a J-R paired star/galaxy catalogue from the APM survey for one field and paired it up with the SuperCOSMOS data. Since the APM data is derived from a copy of the plate that SuperCOSMOS has scanned, any discrepancies in the scanning procedure should be highlighted by this test. Although the measurement of galaxy shapes for the APM machine is different, using density measurements rather than the intensity measurements of SuperCOSMOS, the magnitude cut is low enough that the difference should not matter. Figure 9 shows a scatter plot for individual galaxy ellipticities for a plate on both SuperCOSMOS and APM surveys, and for the binned data, indicating a strong agreement between the surveys.

Having checked for internal and external consistency in the ellipticity catalogue, we now turn to estimating the variance of the ellipticities in cells of varying scale, across all of the plates.

### 3.6 Estimator for the ellipticity variance

The variance of the cell ellipticities can be expressed as the sum of the contributions from all possible sources of alignment (e.g. Bacon et al., 2000)

$$\sigma_{tot}^2 = \sigma_{lens}^2 + \sigma_{int}^2 + \sigma_{noise}^2 + \sigma_{sys}^2 \quad (13)$$

where we have included the contributions from lensing, intrinsic alignments, shot noise and systematics. We assume in what follows that the lensing signal is negligible compared to that from intrinsic alignments for the median redshift of the galaxies in our sample ( $z \approx 0.1$ ). The noise term,  $\sigma_{noise}^2$  is due to intrinsic scatter in galaxy ellipticities and the random error in the measurement of the galaxy ellipticities. Since we are averaging over a very large area of sky (436 plates covering  $\approx 10,000$  sq. degrees with  $\approx 1.7 \times 10^6$  galaxies), we can expect to beat this term down statistically. The final term in equation (13) is due to systematic sources of error. In Section 3.4 we demonstrated the internal consistency of the catalogue, indicating that contributions to this term

<sup>†</sup> available on <http://www.ast.cam.ac.uk/~mike/apmcat/>

from variations in the catalogue are small. Further tests are presented in Section 4.2

We have used a minimum variance estimator for the intrinsic ellipticity variance,  $\sigma_{int}^2$  due to intrinsic alignments in excess of the noise,

$$\sigma_{int}^2 = \frac{\sum_i w_i (e_i^2 - \mathcal{N}_i)}{\sum_i w_i} \quad (14)$$

where  $\mathcal{N}_i$  is the random noise on the estimated cell ellipticity,  $e_i$ , in the  $i^{th}$  cell, and  $w_i$  is an arbitrary weighting factor. We assume that the mean cell ellipticity components are zero (see Section 4.2). For the moment we will ignore systematic terms. Following the analysis of van Waerbeke et al. (2000), we estimate the noise term in the  $i^{th}$  cell as

$$\mathcal{N}_i = \frac{1}{N^2} \left( \sum_{j=1}^N e_{1,j}^2 + \sum_{j=1}^N e_{2,j}^2 \right) \quad (15)$$

where  $N$  is the number of galaxies in the cell.

For a minimum variance estimator, we wish to choose the weights,  $w_i$  such that equation (14) is minimised with respect to  $w_i$ . Denoting the true intrinsic ellipticity variance as  $\sigma_{true}^2$ , this optimal weighting scheme is given by

$$w_i = [\sigma^2(\sigma_{true}^2) + \sigma^2(\mathcal{N}_i)]^{-1} = (2\sigma_{true}^4 + 2\mathcal{N}_i^2)^{-1}, \quad (16)$$

where  $\sigma^2(\sigma_{true}^2)$  is the uncertainty on the true ellipticity variance, and  $\sigma^2(\mathcal{N}_i)$  is the uncertainty on the estimated noise term. Assuming  $\sigma_{true}^2$  to be Gaussian distributed, the uncertainty on the true ellipticity variance will be  $\sigma^2(\sigma_{true}^2) = \sigma_{true}^4$ . The uncertainty in the noise term can be estimated by noting that the noise contribution from randomly orientated galaxies will be  $\mathcal{N}_i = e_{rms}^2/N$  where  $e_{rms}$  is the root mean squared random ellipticity of the galaxies. The variance of the noise is then given by  $\sigma^2(\mathcal{N}_i) = \langle e_g^4 \rangle / N^2 - e_{rms}^4 / N^2$  where  $e_g$  is the ellipticity of the individual galaxies in cell  $i$ . Assuming a Gaussian distribution for the galaxy ellipticities, we can make the approximation,  $\langle e_g^4 \rangle \approx 3\langle e^2 \rangle^2 = 3e_{rms}^4$  and we have  $\sigma^2(\mathcal{N}_i) = 2e_{rms}^4 / N^2 = 2\mathcal{N}_i^2$ . Combining these variances yields the weighting in equation (16). Substituting this into the expression for  $\sigma_{int}^2$  yields the minimum variance estimator:

$$\sigma_{int}^2 = \frac{\sum_i (e_i^2 - \mathcal{N}_i) / (2\sigma_{true}^4 + 2\mathcal{N}_i^2)}{\sum_i (2\sigma_{true}^4 + 2\mathcal{N}_i^2)^{-1}}. \quad (17)$$

The error in this expression is given by

$$\sigma^2(\sigma_{int}^2) = \frac{1}{\sum_i w_i} = \left( \sum_i (2\sigma_{true}^4 + 2\mathcal{N}_i^2)^{-1} \right)^{-1}. \quad (18)$$

Equations (17) and (18) form the basis of our analysis.

## 4 RESULTS

### 4.1 Measurement of the ellipticity variance

We have used equation (17) with  $\sigma_{true} = 0.01$  to calculate the variance of the intrinsic cell ellipticities,  $\sigma_{int}^2$  over a wide range of angular scales. Even so, the results are fairly insensitive to the value of  $\sigma_{true}$  used. We have measured both the b<sub>J</sub> band variance,  $\langle e_i(b_J) e_i(b_J) \rangle$ , and the R band variance,  $\langle e_i(R) e_i(R) \rangle$  as well as the cross-correlation between

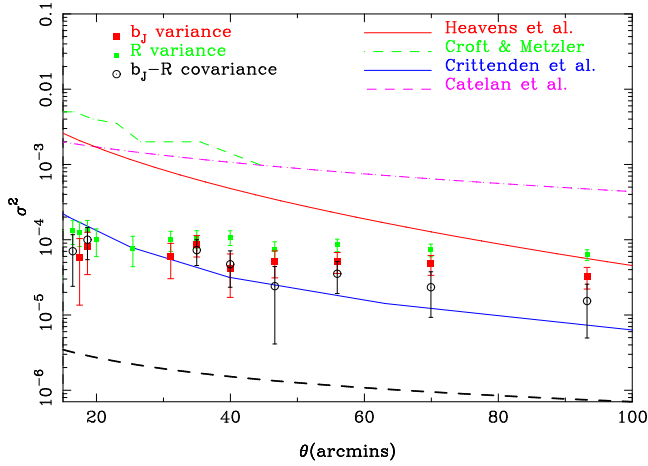


**Figure 10.** Measured ellipticity variance,  $\sigma_{int}^2$  over 436 SuperCOSMOS fields as a function of angular scale,  $\theta$  along with the weak lensing prediction (heavy dashed line) for a  $\Lambda$ CDM model and a median redshift equal to that of our galaxy sample. Also shown are various predictions for the intrinsic signal - see text for details.

the two bands,  $\langle e_i(b_J)e_i(R) \rangle$ . Here, the angled brackets denote the weighted average as in equation (17). Measuring the cross-correlation has the advantage that systematic effects that are uncorrelated between the two bands are cancelled out. The results of all these measurements are shown in Figure 10. In the final analysis, we have made use of  $1.86 \times 10^6$  galaxies for the  $b_J$  band variance,  $1.97 \times 10^6$  for the R band variance and  $1.68 \times 10^6$  for the covariance measurement. Note that the scale at which the stellar ellipticities are smoothed for the PSF anisotropy correction is  $15''$  and so, at scales smaller than this, our results may be compromised by residual PSF anisotropy distortions. We have, therefore, not plotted results below this scale in Figure 10. Beyond this scale, we are confident that our measurements are not dominated by systematics. This assertion is supported by the agreement between the two single band variance measurements and the cross-correlation signal. Further tests for systematics are presented in Section 4.2.

In addition to using equation (18), we have also estimated the errors on our measurements from 1000 randomisations of the dataset. In these randomisations, only galaxies used in the final analysis were included. The galaxies were assigned a position angle taken from a random distribution between 0 and 180 degrees while their semi-major and semi-minor axes were left unchanged. Equation (17) was then used to measure the ellipticity variance from the 1000 randomised datasets. The resulting distributions of 1000 variance measurements are centered on zero at all scales, indicating that our estimator is unbiased. These distributions are shown in Figure 11, along with the measured signal, for four scales: 19, 40 and 56 and 93 arcmins. The errors on the signal measured from the real dataset were then calculated as the standard deviation of the measurements from the randomised catalogues. These errors agree quite well with the errors calculated using equation (18) although those taken from the randomisations are, in general, slightly larger. We have therefore plotted the  $1\sigma$  errors from the randomisations in Figure 10.

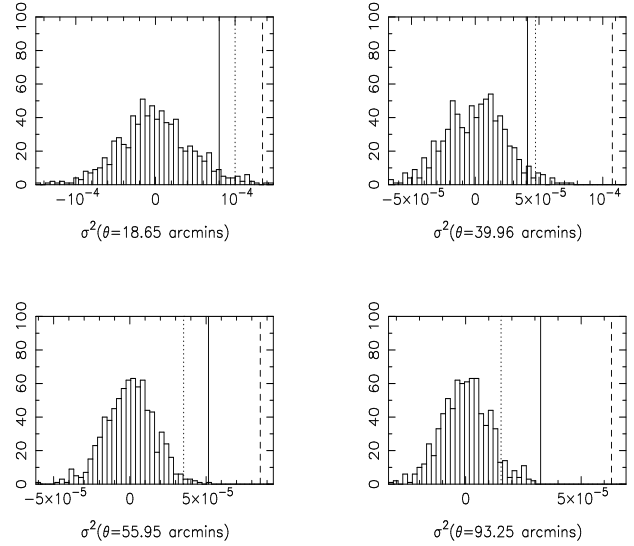


**Figure 11.** The variance measurements from the 1000 randomised catalogues (histograms) along with the measured signal for four different values of the cell side length,  $\theta$ . In each case, the full line is the  $b_J$  band variance, the dashed line is the R band variance and the dotted line is the covariance measured between the two bands.

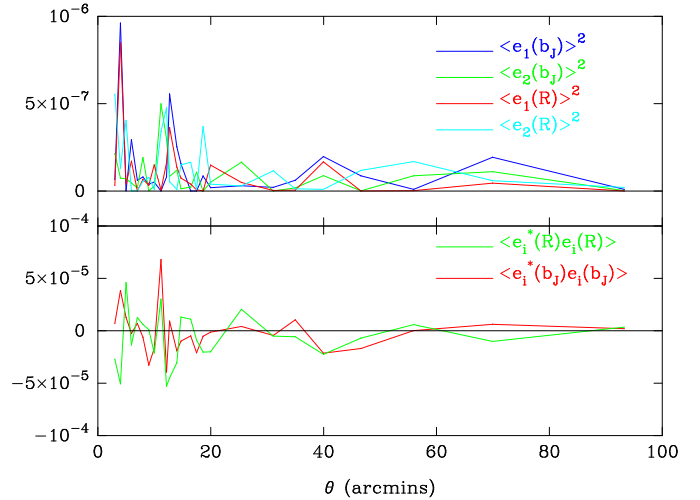


**Figure 12.** Top panel: The average galaxy ellipticity components,  $\langle e_\alpha \rangle^2$  over the 436 SuperCOSMOS plates for the  $b_J$  and R bands. Bottom panel: The star-galaxy covariance,  $\langle e_i^* e_i \rangle$  measured over the whole survey for the two bands.

Our measurements are two orders of magnitude larger than the signal expected from weak lensing (see e.g. Jain & Seljak, 1997) for a median source redshift of  $z \approx 0.1$  corresponding to the magnitude cut of  $b_J \leq 20.5$  which we have used in our analysis. In Figure 10 we plot our results along with the predicted weak lensing signal for a cluster normalised  $\Lambda$ CDM model, with  $\Omega_m = 0.3$  and  $\Omega_\Lambda = 0.7$ . The discrepancy is exhibited over the entire range of angular scale,  $\theta$  suggesting that we have not measured extrinsic gravitational lensing.

#### 4.2 Tests for systematics

To test our results for internal systematics we have estimated the means of the cell ellipticity components averaged

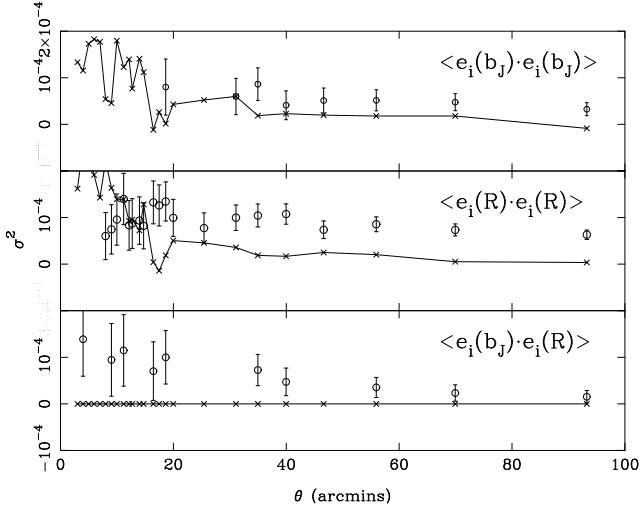


**Figure 13.** The signal measured (points with error bars) in  $b_J$  (top),  $R$  (middle) and the cross-correlation between the two bands (bottom) along with the cross correlation of  $e_1$  with  $e_2$  for the galaxies,  $\langle e_1 e_2 \rangle$  (joined crosses). Note the much higher significance of the shear covariance measurement,  $\langle e_i(b_J) e_i(R) \rangle$  compared with the shear variance measurements from the individual bands alone.

over all plates. In Figure 12 we show that the mean fields are negligible ( $\langle e_\alpha \rangle^2 < 10^{-7}$ ) on all scales. We have also estimated the star-galaxy covariance,

$$\langle ee^* \rangle = \langle e_1 e_1^* \rangle + \langle e_2 e_2^* \rangle, \quad (19)$$

where  $e^*$  is the stellar ellipticity. This is also shown in Figure 12, and is well below our results ( $|\langle ee^* \rangle| < 10^{-5}$ ) on all scales, indicating that, after applying the cut on galaxy size (Section 3.2), galaxy ellipticities are no longer correlated with stellar values. We have estimated the cross-correlation of  $e_1$  and  $e_2$  for the galaxies,  $\langle e_1 e_2 \rangle$ . This is plotted in Figure 13 along with the measured signal for the two single band variance measurements as well as for the shear covariance signal. In all cases, the galaxy cross correlation,  $\langle e_1 e_2 \rangle$  is consistently below the measured signal. In particular, for the covariance measurement, we have estimated the galaxy cross correlation as

$$\langle e_1 e_2 \rangle = \langle (e_1(b_J) e_2(R) + e_1(R) e_2(b_J)) / 2 \rangle \quad (20)$$

and this is consistent with zero at the  $10^{-9}$  level on all scales, indicating that  $\langle e_i(b_J) e_i(R) \rangle$  is free of significant residual systematics and is a robust estimate of the galaxy alignment signal.

As a test for systematics introduced by the measuring process we have pushed the APM data (Section 3.5) through our analysis for one plate. In Figure 14 we plot the variance as measured by the two machines for this field. Again we find a very good agreement between both catalogues, suggesting that any systematic effects in our analysis are small,  $\sigma_{\text{sys}}^2 < 10^{-5}$ , and below our measurement. This agreement between the catalogues is demonstrated in Figure 15 where the difference in variance measurements from the two surveys is plotted. This difference is consistent with zero on all scales.

As noted in Section 3.1, the SuperCOSMOS machine measures unweighted second moments of all objects detected within an isophotal threshold,  $I_{th}$ . The nominal value of this threshold in the SuperCOSMOS Sky Survey is  $2.3\sigma$  above

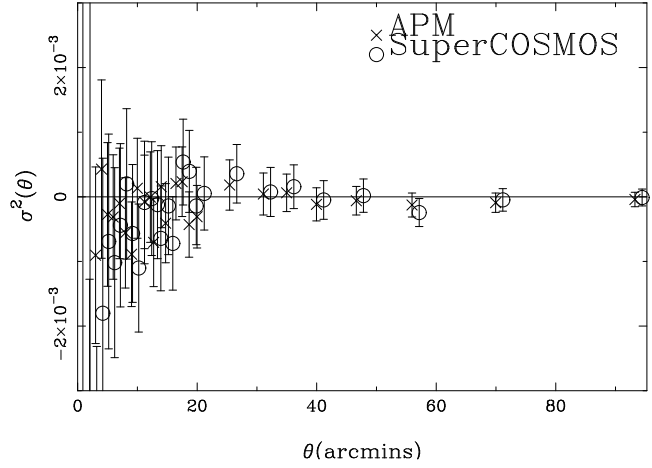


**Figure 14.** Comparison of the SuperCOSMOS variance of ellipticities and the APM variance for one plate (UKST field 78). Note the errors are much larger than in the final analysis due to the much smaller number of galaxies measured. The SuperCOSMOS points have been slightly laterally displaced for clarity.

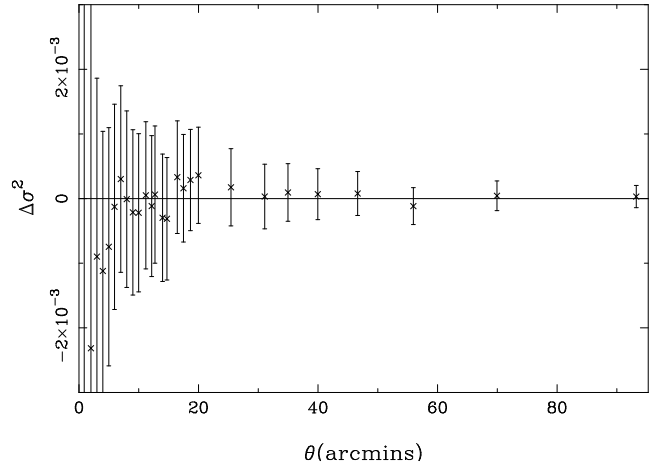


**Figure 15.** The difference in the ellipticity variance as measured from the SuperCOSMOS and APM machines ( $\Delta\sigma^2 = \sigma_{apm}^2 - \sigma_{scos}^2$ ) for the same field as shown in figure 14. The value of  $\Delta\sigma^2$  is consistent with zero on all scales indicating that systematic errors introduced by the plate scanning procedure are small.

the sky background,  $I_{sky}$ . To further establish the reliability of our ellipticity measurements, we have varied  $I_{th}$  about its nominal value for one field and compared the resulting galaxy ellipticity measurements with those from the main analysis for this field. The results of this test are shown in Figure 16 showing that the determination of the galaxy ellipticities is largely insensitive to the isophotal threshold used to measure the object parameters.

### 4.3 Intrinsic alignments

Recent numerical and analytic studies (Catelan et al., 2001; Crittenden et al., 2001; Croft & Metzler, 2001; Heavens et al., 2000) have put constraints on the shear signal expected from intrinsic galaxy alignments. In these studies the galaxy shape is estimated either from the perpendicular to the halo angular momentum vector for spirals, or from the shape of the halo for ellipticals.



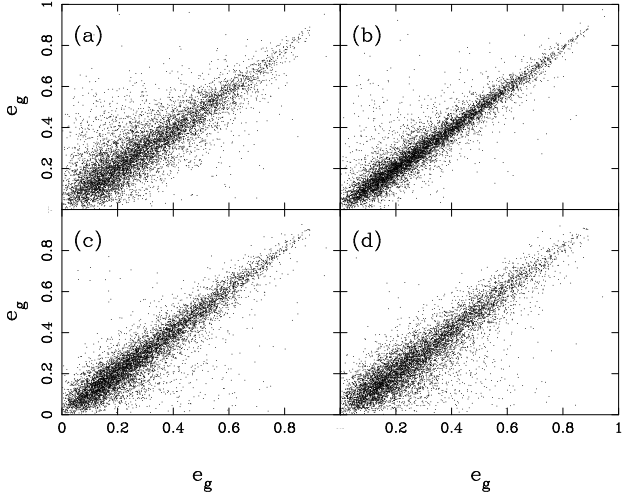


**Figure 16.** Individual galaxy ellipticities as measured from UKST field 78 with different isophotal thresholds applied. In each of the four panels, the horizontal axis measurements are from the Sky Survey data with an isophotal threshold value of  $2.3\sigma$  above the sky background. The vertical axes measurements have been made using isophotal threshold values of (a)  $1.5\sigma$ , (b)  $2.0\sigma$ , (c)  $3.5\sigma$  and (d)  $4.5\sigma$  above the sky background.

In Figure 10 we have plotted our results along with the alignment effect estimated from each group. Also shown are results from an extension to the numerical simulations work of Heavens et. al., 2000 for the spiral galaxy model at  $z = 0.1$  (A. Heavens, private communication). The spread in models can be accounted for by the choice of mechanism and galaxy type, assumptions about alignments between halos and galaxies, correlations between tidal and inertial fields and disc thicknesses. We have used the redshift scaling  $z^{-2n}$ , suggested by Crittenden et al., where  $n$  is the slope of the matter correlation function, to scale the results from different redshifts. We have also assumed  $\sigma^2(\theta) = 2/(2-n)C(\theta)$ , where  $C(\theta)$  is the ellipticity correlation function.

Generalising the arguments by Crittenden et al. (2001), at large scales the ellipticity variance should scale as

$$\sigma^2(\theta) \approx Az^{-2n}|1 + (\theta/\theta_0)^2|^{-n}. \quad (21)$$

One would hope that with future, more precise observations of intrinsic alignments, it may become possible to constrain the slope of the matter correlation function, and thus shed light on the clustering properties of dark matter on these scales ( $\leq 10 h^{-1}\text{Mpc}$ ).

## 5 CONCLUSION

In this paper we have presented a measurement of the intrinsic alignment effect of galaxies on scales from a few arcminutes to 100 arcminutes. Using 2 million galaxy ellipticities measured from the digitized SuperCOSMOS Sky Survey, to a depth of  $b_J = 20.5$  and median redshift  $z = 0.1$  and covering 436 plates or 10,000 sq. deg. in two passbands, we have corrected the data for distortions due to PSF anisotropy and seeing, and applied a new minimum variance estimator to the data.

After applying these corrections to the dataset and

excluding the over-corrected small galaxies, we find our measurements are internally consistent, with good agreement in regions where the plates overlap, with effectively zero star-galaxy ellipticity correlations and zero  $e_1$ - $e_2$  cross-correlations. The ellipticity variance measurements from the  $b_J$  and R passbands agree well with each other and with the cross-correlation between the two bands — further confirmation that systematic effects are small. We have also demonstrated external consistency with the APM sky catalogue data over a restricted region of sky, indicating that we are not contaminated by measurement systematics.

Our resulting estimates of the ellipticity variance over a wide range of scales are two orders of magnitude higher than that expected from gravitational lensing by large-scale structure, but roughly in line with those predicted from intrinsic alignments in the gravitational instability scenario, although the predictions for intrinsic alignments are still uncertain. For instance, it is not clear if the effect is dominated by tidal spin or shape alignments. This agreement suggests that we are not contaminated by internal systematics.

Our results imply that other shallow surveys, such as the Sloan Digital Sky Survey, should measure roughly the same contribution to the total variance from intrinsic alignments and gravitational lensing shear. Since the intrinsic alignment signal is expected to scale as  $z^{-2}$  (Crittenden et al., 2001) and the lensing signal as  $z^{1.5}$  (Jain & Seljak, 1997), we expect the ratio of intrinsic alignment to gravitational shear to scale as

$$\frac{\sigma_{int}^2}{\sigma_{lens}^2} \approx 10^2 \left( \frac{z}{0.1} \right)^{-3.5}. \quad (22)$$

This ratio is unity at around  $z \approx 0.37$ . Higher redshift surveys, such as the VISTA Gravitational Lensing Survey (Taylor, 2001) with  $z \approx 1$ , will measure gravitational lensing shear.

While one would hope that the correlations between ellipticity, spin and the shear field would allow one to measure the amplitude of the dark matter density field, the spin is also determined by the inertial tensor of the dark matter halo. At present, the relation between shape and the local shear field of haloes, and the relationship between galaxy ellipticity and halo shape, introduces a large uncertainty in our understanding of intrinsic ellipticity alignments. With present and future observations and theory we can hope to resolve these issues.

## ACKNOWLEDGEMENTS

MLB thanks the University of Edinburgh for a studentship. SD thanks the PPARC for a PDRA grant, and the Institute for Astronomy, Edinburgh for support during the writing of this paper. ANT is a PPARC Advanced Fellow. MLB and ANT thank Alan Heavens, Rob Crittenden, Lance Miller, David Bacon and Alex Refregier for useful discussions about intrinsic alignments and weak shear measurements. The authors thank the Institute for Astronomy's Wide Field Astronomy Unit for assistance in this project.

## REFERENCES

Bacon D., Refregier A., Ellis R., 2000, MNRAS, 318, 625

- Bartlemann M., Schneider P., 1999, Review for Physical Reports (astro-ph/9909155)
- Catelan P., Kamionkowski M., Blandford R.D., 2001, MNRAS, 323,713
- Crittenden R., Natarajan P., Pen-U., Theuns T., 2001, ApJ, 559, 552
- Croft R.A.C., Metzler C.A., 2001, ApJ, 545, 561
- Gray, M.E. et al., 2001, ApJ (accepted)
- Heavens A.F., Refregier A., Heymans C., 2000, MNRAS, 319, 649
- Hambly N.C., et al., 2001a, MNRAS, 326, 1279
- Hambly N.C., Irwin M.J., MacGillivray H.T., 2001b, MNRAS, 326, 1295
- Hambly N.C., Irwin M.J., Davenhall, A.C., MacGillivray H.T., 2001c, MNRAS, 326, 1315
- Hoyle, F., 1949, in Burgers J.M., van de Hulst H.C., eds., in Problems of Cosmic Aerodynamics, Central Air Documents, Dayton, Ohio, p195
- Jain B., Seljak U., 1997, ApJ, 484, 560
- Kaiser N., Wilson G., Luppino G., 2000, submitted to ApJL (astro-ph/0003338)
- Kaiser N., Squires G., Broadhurst T., 1995, ApJ, 449, 460
- Kamionkowski M., Babul, A., Cress, C.M., Refregier, A., 1998, MNRAS, 301,1064
- Knox, R.A.,Hambly, N.C., Hawkins, M.R.S., MacGillivray, H.T., 1998, MNRAS, 297, 839
- Pen U-L., Lee J., Seljak U., 2000, ApJ, 543, L107
- Stobie, R.S., 1986, Pattern Recognition Letters 4, 317
- Taylor, A.N., 2001, to appear in Treyer & Tresse, eds., Where's the Matter? Tracing Bright and Dark Matter with the New Generation of Wide Field Surveys, Frontier Group
- van Waerbeke L., et al, 2000, A&A, 358, 30
- Wallace, P.T., Tritton, K.P., 1979, MNRAS, 189, 115
- Wittman D.M., Tyson J.A, Kirkman D., Dell'Antonio I., Bernstein G., 2000, Nature, 405, 143
- Wynne, C.G., 1981, Q. Jl. RAS, 22, 146